Available online at www.sciencedirect.com

jmr&t Journal of Materials Research and Technology

journal homepage: www.elsevier.com/locate/jmrt

Original Article

Microstructure and fatigue properties of extruded aluminum alloys 7046 and 7108 for automotive applications

C.S. Hattori [a], G.F.C. Almeida [a,b,*], R.L.P. Gonçalves [b], R.G. Santos [c], R.C. Souza [c], W.C. da Silva Jr. [d], J.R.C. Cunali Jr. [b], A.A. Couto [a,b]

[a] Instituto de Pesquisas Energéticas e Nucleares - IPEN, São Paulo, Brazil
[b] Universidade Presbiteriana Mackenzie - UPM, São Paulo, Brazil
[c] Instituto Federal de Educação e Ciências e Tecnologia de São Paulo - IFSP, São João da Boa Vista, SP, Brazil
[d] Instituto Federal de Educação e Ciências e Tecnologia de São Paulo - IFSP, Guarulhos, SP, Brazil

ARTICLE INFO

Article history:
Received 10 July 2021
Accepted 21 August 2021
Available online 28 August 2021

Keywords:
Fatigue
Aluminum alloys
AA7108
AA7046
Extrusion

ABSTRACT

This work aimed to obtain by extrusion two aluminum alloys, 7108 and 7046. The microstructural characterized at each stage of the manufacturing process and the mechanical fatigue behavior of the extruded profile were evaluated. The aluminum alloys in the as-casted condition exhibited an interdendritic microsegregation inside the grains, with intermetallic phases precipitated on the grain boundaries. In the homogenization of the billets of the AA7108 and AA7046, the precipitated phases dissolved. The AA 7046, in the as-casted condition, displayed shrinkage microvoids throughout the length of the billet and a microstructure of heterogeneous grains, with the presence of a remelted layer at a maximum depth of 10 mm. The AA7046 displayed better tensile and fatigue properties than the AA7108. A higher surface roughness facilitated the initiation and propagation of cracks during the fatigue cycles. This effect was more pronounced with low levels of maximum stress and high number of cycles to failure. Deep secondary cracks perpendicular to the growth direction of the main crack were visible on all fracture surfaces. In the medium and high cycle fatigue tests of the AA7108 and AA7046, the cracks advanced in a perpendicular direction to the elongated grains resulting from the extrusion process. The fracture surfaces of the tested samples with a high number of cycles exhibited a region with a smaller crack propagation area and a larger region of rupture due to mechanical overload. The region of crack propagation is characterized by plastic deformation and the presence of striations perpendicular to the growth direction.

© 2021 The Authors. Published by Elsevier B.V. This is an open access article under the CC BY-NC-ND license (http://creativecommons.org/licenses/by-nc-nd/4.0/).

* Corresponding author.
E-mail address: gisele_fab@hotmail.com (G.F.C. Almeida).
https://doi.org/10.1016/j.jmrt.2021.08.085
2238-7854/© 2021 The Authors. Published by Elsevier B.V. This is an open access article under the CC BY-NC-ND license (http://creativecommons.org/licenses/by-nc-nd/4.0/).

1. Introduction

Vehicle weight is constantly increasing due to increasing safety, luxury, and performance features. However, the automotive industry must still comply with increasingly stringent fuel efficiency and emissions standards. The application of aluminum-based automotive components is considered one of the most promising ways to resolve these conflicting developments. For application in safety and impact-absorbing components, the combination of a high-strength alloy with the appropriate design (infinite possibilities of geometry in extruded profiles) further enhances the formability and ductility characteristics of aluminum and its alloys.

The focus on lightness suggests the use of higher strength aluminum alloys of the 7XXX series. These alloys are mostly made of Al–Zn–Mg or Al–Zn–Mg–Cu, and these alloying elements increase the mechanical strength. The 7XXX series alloys have phases that are balanced with the matrix rich in aluminum, with the ability to be solubilized and precipitated. The most common in this system include the η or M phases ($MgZn_2$), T ($Al_2Mg_3Zn_3$), and the beta phase (Al_3Mg_5). The addition of Mg to Al–Zn alloys could greatly increase the mechanical strength of this system, especially the range of 3–7.5% Zn, which combines with Mg to form $MgZn_2$ (phase η). The $MgZn_2$ precipitate is the main intermetallic compound responsible for the age hardening of these alloys. Most research about the 7XXX series aluminum alloys has focused on alloys such as AA7075 and AA7050. Several of these works specifically study the obtainment, processing, microstructural characterization, and mechanical behavior in fatigue [1–4]. These 7XXX series alloys feature very high ultimate tensile strength. However, the advantage of high strength is accompanied by relatively low elongation at the fracture. One way to change the mechanical properties of the 7XXX series alloys is to use suitable alloying elements and thermomechanical treatments.

Several studies have been done on 7xxx series aluminum alloys after hot deformation [5–9]. Gupta et al. [5] observed a dynamic recrystallization was found to have significant role in governing the hot deformation behavior of the 7010 and 7075 aluminum alloys. According to Jin et al. [6], in the deformed at elevated temperature structures appear the elongated grains with serrations developed in the grain boundaries. Mirzadeh [7,8] studied the hot work behavior of 7075 aluminum alloys through constitutive analysis based on the apparent and the proposed physically-based approach. This author concluded that this approach can be considered a versatile tool in future comparative hot work studies, especially in studies dedicated to the development of alloys. The effects of grain size on hot deformation and processing map of 7075 aluminum alloy were investigated by Yang et al. These authors concluded that the optimized hot work parameters of 7075 aluminum alloy with different grain sizes can be used in various hot work processes.

New Cu-free 7XXX series aluminum alloys with small amounts of Zr and Ti have been investigated as promising candidates in automotive applications that combine good mechanical and fatigue strength associated with excellent corrosion resistance [10–12]. Aluminum Alloys 7108 and 7046 are relatively new and few studies have specifically examined their manufacturing processes and mechanical properties [13]. Given this and the potential use of these alloys in automotive applications, this work will focus on the obtainment, microstructural characterization, and mechanical fatigue behavior of these alloys. The objectives of the work are to obtain by extrusion the aluminum alloys 7108 and 7046, characterize microstructures at each stage of the manufacturing process, and evaluate the mechanical fatigue behavior of samples with the extruded profile.

2. Materials and methods

This work used billets made of AA7108, produced by vertical casting technology, and AA7046, produced by horizontal casting, all with a diameter of 203.2 mm. Table 1 provides the chemical compositions of the alloys studied. Chemical composition analyzes were performed by wavelength dispersion X-ray fluorescence spectrometry, employing a Thermo Scientific spectrometer – ARLs 3460. Differences in the chemical composition of aluminum alloys could be observed, with AA7046 presenting higher levels of alloying elements than AA7108, which affected the entire process of homogenization, extrusion, and heat treatments, as well as the mechanical properties of the alloys.

The cast billets were homogenized to increase efficiency in the extrusion process, guaranteeing mechanical properties in the plastic deformation process, a better surface finish of the profile, and a longer useful life of the matrix. The homogenization heat treatment of billets for AA7108 was conducted at 485 °C for 10 h and for AA7046 at 470 °C for 12 h. Heating was performed at a low rate to ensure maximum compound dissolution and redistribution of solutes in the matrix. At the end of homogenization, the billet was cooled at a moderate rate to favor the retention of some solutes in the Al matrix and so that the precipitated phases would distribute along the billet. After the homogenization heat treatment, the billet ends were discarded to eliminate the impurities that are normally found in these regions.

The extrusion process in a press with a pressure capacity of 280 bar obtained tubular profiles with cross sections illustrated in Fig. 1. After extrusion, the profiles went through the stretching process with 0.3% strain to improve straightness

Table 1 – Chemical analysis of the AA7108 and AA7046 in percentage by mass.

Alloy	Si	Fe	Mg	Mn	Zn	Cu	Cr	Ti	Zr	Balance
7108	0.04	0.08	0.8	0.002	4.5	–	0.002	0.02	0.16	94.3
7046	0.10	0.14	1.3	0.004	6.5	0.16	0.004	0.05	0.15	91.5

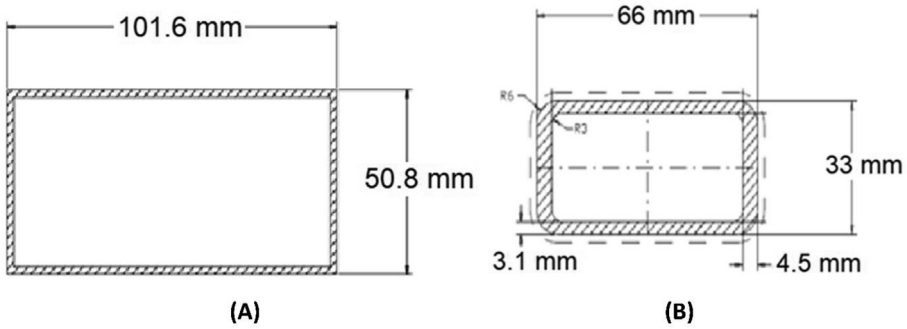

Fig. 1 – Cross section of extruded profiles of aluminum alloys (A) 7108 and (B) 7046.

along the length and for the cutting process. As the friction force between the billet and the container wall depends on the contact area between them, a reduction in the length of the billet considerably reduces the friction force, so a larger portion of the extrusion force can be used to overcome the shear. The more alloying elements in the chemical composition, the greater the shear force to overcome; therefore, smaller billets are more recommended in these cases. For this reason, for the experiments on AA7108 and AA7046, 500 mm long billets were chosen.

The AA7108 billets were maintained at a temperature of 420 °C. The receptacle temperature was maintained at 400 °C and the emerging temperature at 470 °C. The extrusion speed of this alloy was 2.5 m/min, with water spray cooling. This alloy exhibited good fluidity in the extrusion process, because the stability of the emerging temperature of the profile provided good solubilization. The container temperature remained constant throughout the process, also contributing to the stability of the emergent temperature. Other factors that evidenced this were the extrusion pressure, which reached a maximum of 181 bar, and the consistency of the tool temperature. A relative loss of tool temperature can cause overload of the equipment due to high working pressure, in addition to surface defects along the profile, which were not detected. The surface quality of the profile was indicated by the absence of defects and cracks along the length of the profile.

The billets of the AA7046 were maintained at a temperature of 470 °C. The press pressure was 210 bar throughout the process. The container temperatures were around 450 °C and the emerging temperature was 510 °C. The extrusion speed of this alloy was 1.5 m/min, with water spray cooling. Despite the greater extrusion complexity, the press pressure for this alloy (210 bar) was higher than the profile extrusion pressure for the AA7108, due to the greater amount of alloying elements. The extruded profile of AA7046 also displayed good surface quality, without any cracks or apparent defects.

To obtain productivity in the process with a good level of product quality for the two alloys, the extrusion speed was controlled, together with the working temperature of the billets. The faster extrusion speed causes more violent deformation of the metal flowing through the matrix and generates more heat, and therefore a greater increase in the emergent temperature. Maintaining the billets with a temperature gradient one of the devices employed, in which the billet has a temperature differential between its tip, middle, and end, with the tip having a higher temperature than the others. For this reason, the temperature of the billets varied within a range. After extrusion and solubilization, the alloys were aged using the following conditions: 150 °C for 20 h for the AA7108 and 155 °C for 17 h for the AA7046. These conditions for solubilization and ageing achieved the best hardness and tensile test results.

Optical microscopy, with and without polarized light, and scanning electron microscopy (SEM) were employed for microstructural characterization of the alloy. The samples were taken from the periphery, mid-radius, and center regions of the cross section of the billets and in the longitudinal section of the heat-treated extruded bars. The metallographic samples were prepared using conventional sanding, polishing, and chemical etching techniques with an aqueous solution of fluoboric acid (HFB_4), followed by anodization for 3 min. Observations by optical microscopy were done on an Olympus BX51 microscope. SEM analyzes were performed in a FEI Quanta 450 microscope.

Hardness measurements were performed on a Tinus Olsen bench-top durometer, model FH_001. The tensile tests were carried out in a universal mechanical testing machine EMIC, model DL 10000. The fatigue tests were conducted on an Instron 8801 equipment, with a load capacity of 100 kN. The fatigue tests for both alloys were performed with $R = 0.1$ and maximum tensions ranging from 30 to 70% of the ultimate tensile strength (UTS). The fatigue tests were conducted in ambient air temperature at a nominal frequency of 20 Hz. For each applied stress cycle, 4 fatigue tests were carried out. The sample used for the tensile and fatigue tests is illustrated in Fig. 2. The fracture surfaces of the samples in fatigue tests were observed by SEM. The surface roughness of the fatigue test samples was analyzed with the aid of a Mitutoyo roughness tester, model SJ-30. In each sample, the procedure was performed in the thickness and width of the reduced section. Roughness was measured on the R_a, R_z, and R_q scales.

3. Results and discussion

Figs. 3 and 4 are typical micrographs of the periphery region of the AA7108 billet in the as-casted and homogenized

Fig. 2 – Specimen for tensile and fatigue tests machined from extruded profiles of AA7108 and AA7046.

conditions, respectively. Fig. 3(A) illustrates the geometry and size of the grains, characteristic of the uniform heat extraction rate at the periphery of the billet. The interdendritic microsegregation inside the grains is evidenced by the difference in color from the center of the grains to the ends, with a characteristic geometry of dendritic growth. Due to the low speed of solidification practiced, the solutes were pushed to the solidification front, as visible in Fig. 3(B). Consequently, the precipitated phases are almost completely at the grain boundaries of the α-Al phase.

Fig. 4 indicates that when the billet was homogenized, the phases concentrated in the grain boundaries were dissolved by heating, and the chemical elements resulting from this dissolution were solubilized in the α-Al phase upon cooling.

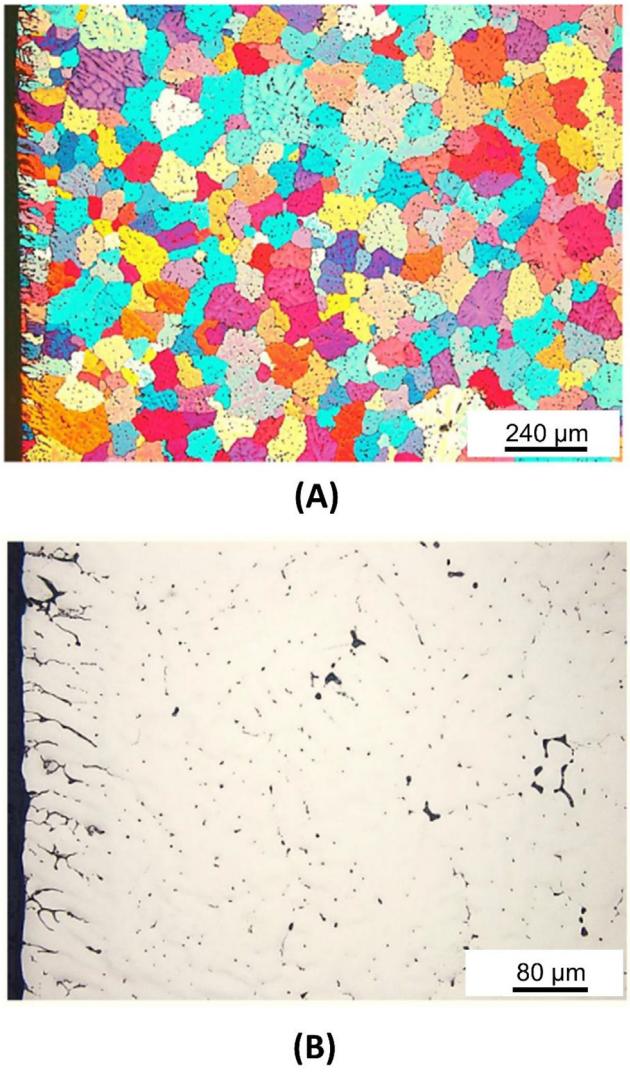

Fig. 3 – Periphery micrograph of the cross section of the AA7108 billet in the as-casted condition. (A) Chemically etched and anodized micrograph and (B) without etching.

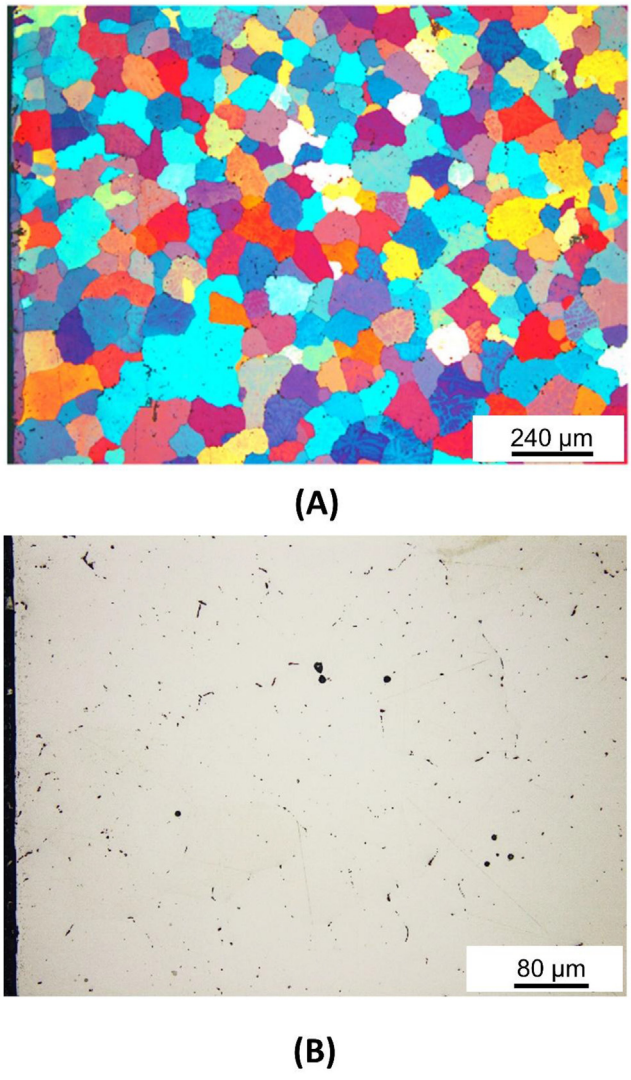

Fig. 4 – Periphery micrograph of the cross section of the AA7108 billet in the homogenized condition. (A) Chemically etched and anodized micrograph and (B) without etching.

With solubilization of a large quantity of elements in the Al matrix in the homogenized condition, a smaller quantity of precipitated phases in the matrix and with smaller size was observed than in the as-casted condition. Furthermore, the precipitates in the homogenized condition were more homogeneously distributed in the billet.

The micrographs in the mid-radius and central positions of the billet exhibited a microstructure similar to that observed in the edge, both in the as-casted and homogenized conditions. The second phase particles in the regions of the grain boundaries have the same morphology and distribution as those observed at the edge of the billet. Furthermore, cracks occurred due to solidification in the central region of the billet, as this is the region most stressed by solidification. Solidification stresses in the central region of the billets occur mainly in alloys with high content of alloying elements, as they cause an increase in the shrinkage rate during aluminum solidification, as was the case of the AA7108, which contained a high content of Zn.

The SEM and energy dispersive spectroscopy (EDS) analyzes of the AA7108 identified the presence of Al_3Zr and $AlFe_3$/Al_8FeSi_2 precipitates in the as-casted condition. The addition of Zr to form the Al_3Zr precipitate is due to its ability to inhibit grain growth, increasing the recrystallization temperature [14]. Fig. 5 presents the micrograph obtained by SEM of the central region of the homogenized AA7108 billet. This figure displays the presence of only $AlFe_3$/Al_8FeSi_2 precipitates in the grain boundaries. The homogenization, in addition to altering the precipitates of the $AlFe_3$/Al_8FeSi_2 phases, also promoted the complete solubilization of Al_3Zr.

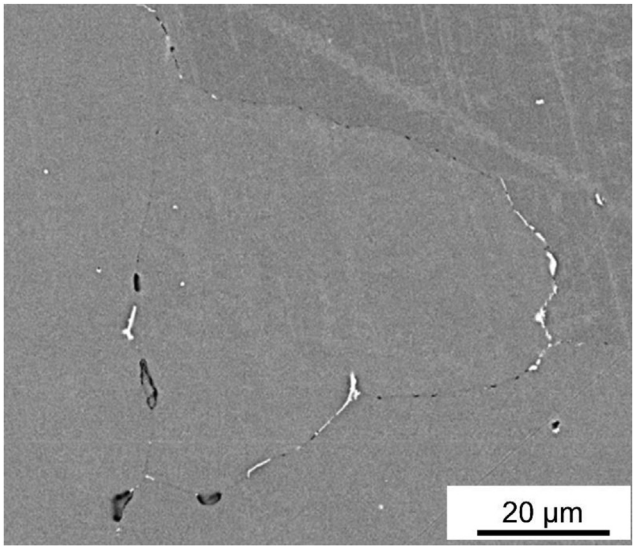

Fig. 5 – Microstructure of the central region of the cross section of the AA7108 billet with homogenization treatment.

The microstructure of the periphery region of the AA7046 billet in the as-casted condition is visible in Fig. 6. The micrograph of Fig. 6 evidences the micro-shrinkage voids present throughout the length of the sample and a heterogeneous grain microstructure, with the presence of the remelted layer at a maximum depth of 10 mm. In Fig. 7, the typical micrographs of the regions of the half radius and the center of the billet are presented in the as-casted (7(A)) and homogenized (7(B)) conditions. The images generated after electrolytic etching by anodizing reveal a microstructure with a homogeneous grain distribution, unlike that observed on the edge of the billet.

In the AA7108, as in the AA7046, precipitated phases of $AlFe_3$/Al_8FeSi_2 were also identified in the aluminum matrix both in the as-casted and homogenized conditions. The particles containing Fe remained insoluble during the homogenization heat treatment. The coarse η-phase ($MgZn_2$) precipitates in AA7046 were dissolved during the homogenization treatment. According to the works of Xu et al. [15–17], this is due to the low temperature solvus of the η phase and the relatively fast diffusivity of Mg and Zn. Fig. 8 illustrates the micrograph obtained by SEM of the central region of the homogenized AA7046 billet. In the AA7046, the volume of $AlFe_3$/$Al8FeSi_2$ second phase particles increased because this alloy had a higher concentration of Fe and Si (not soluble in aluminum) than the AA7108.

After homogenization, the billet was reheated to 480 °C to enable its hot extrusion. In addition to a pronounced increase in billet formability, the precipitates were redissolved, and the alloying elements were again solubilized in the Al matrix. Then, the solubilized profile was subjected to the aging heat treatment. Figs. 9 and 10 present the micrographs of the longitudinal section of the extruded bars of the AA7108 in its solubilized and artificially aged condition. Fig. 9 illustrates the microstructure of elongated grains along the length of the extruded profile is presented. As noted in a previous work [18], the material is highly textured, with the grains severely elongated in the (111) and (200) orientation of the planes along the direction of extrusion. Fig. 9 also exhibits subgrains within

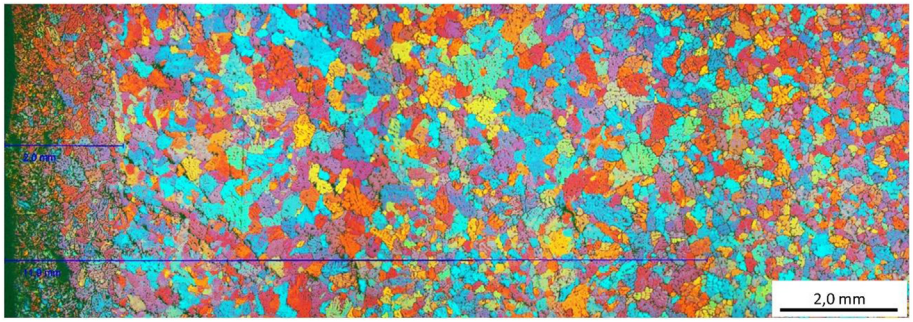

Fig. 6 – Microstructure of the edge of the cross-section of the AA7046 billet in the as-casted condition.

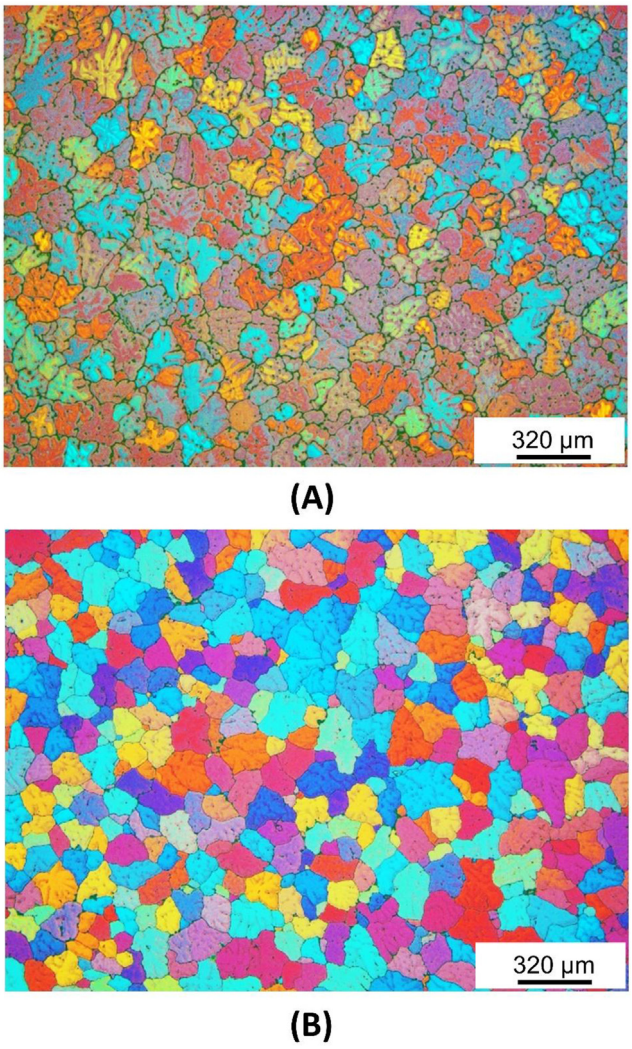

Fig. 7 – Microstructure of the mid-radius region of the cross section of the AA7046 billet in the (A) as-casted and (B) homogenized conditions.

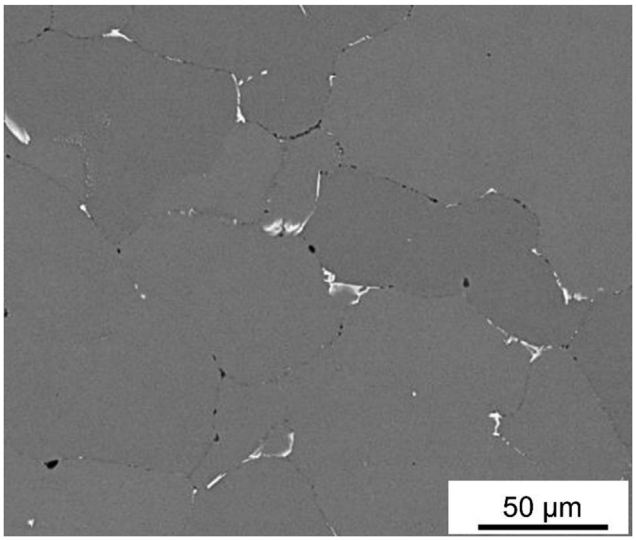

Fig. 8 – Image viewed through backscattered electrons of the central region of the cross section of the AA7046 billet after homogenization heat treatment.

the elongated initial grains arranged in rows parallel to the direction of extrusion. This microstructure also displays the presence of recrystallized grains on the upper surface with a maximum depth of 35 μm.

In Fig. 10, the dark field image by optical microscopy of a sample of the extruded profile of the AA7108 evidences the presence of fine $MgZn_2$ precipitates and second-phase particles of $AlFe_3/Al_8FeSi_2$ dispersed in the aluminum matrix. Furthermore, these Al–Fe–Si particles are oriented along their long axis parallel to the direction of extrusion. In the SEM analysis of the extruded profile of the AA7108, second-phase contrast particles of $AlFe_3/Al_8FeSi_2$ (clear particles) are observed, as seen in Fig. 11.

Fig. 12 presents the sample micrograph of the AA7046 exhibiting a microstructure with elongated grains and recrystallized grains on the surface at a maximum depth of less than 50 μm, similar to that observed in the AA7108. The microstructure is typical for extruded aluminum alloys with homogeneous distribution of constituents, phases rich in second phase particles. In the dark field image of this profile sample, in Fig. 13, notice the presence of fine $MgZn_2$ precipitates and $AlFe_3/Al_8FeSi_2$ second-phase particles dispersed in the aluminum matrix and in greater amounts than in the AA7108.

The values for yield strength (YS), ultimate tensile strength (UTS), and elongation (E) obtained in tensile and Brinell hardness (BH) tests of AA7108 and AA7046 samples in the solubilized and aged condition are presented in Table 2. As mentioned above, the results of the tensile and hardness tests in Table 2 were obtained under the optimized conditions for solubilization and aging for each of the two alloys. Both alloys achieved increased mechanical strength with aging time until

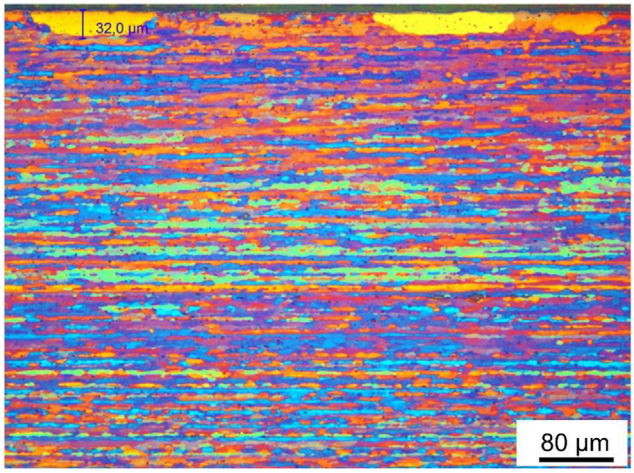

Fig. 9 – Micrograph observed with polarized light of a sample of the longitudinal section of the extruded profile of the solubilized and aged AA7108.

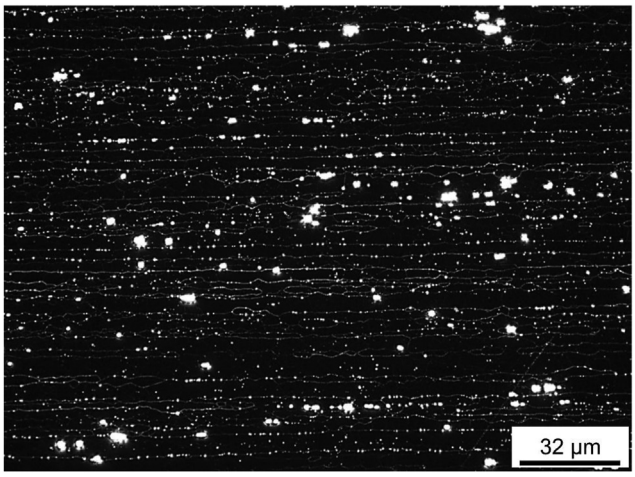

Fig. 10 – Dark field micrograph of the longitudinal section of a sample of the extruded profile of solubilized and aged AA7108.

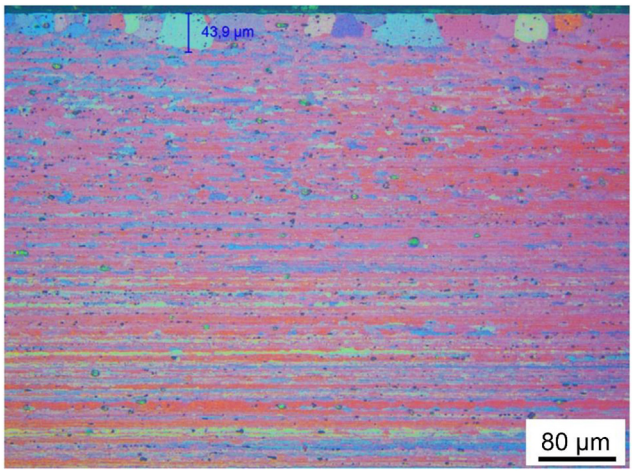

Fig. 12 – Micrograph observed with polarized light of a sample of the longitudinal section of the extruded profile of solubilized and aged AA7046.

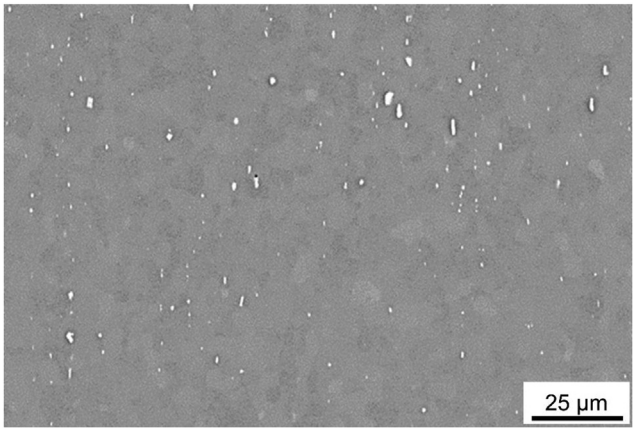

Fig. 11 – Image observed through backscattered electrons in a scanning electron microscope of the longitudinal section of a sample of the extruded profile of the solubilized and aged AA7108, showing light particles of $AlFe_3/Al_8FeSi_2$.

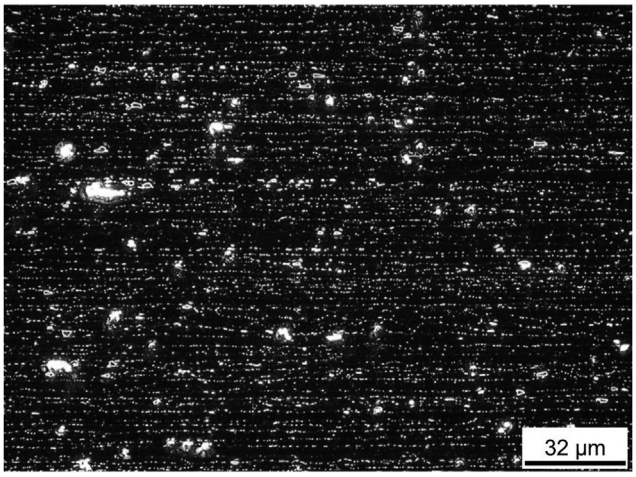

Fig. 13 – Dark-field micrograph of the longitudinal section of an extruded profile of a solubilized and aged AA7046.

reaching the peak strength. The peak was reached with 20 h of aging at 150 °C for the AA7108 and 17 h at 155 °C for the 7046. The AA7046 had greater mechanical strength values than the AA7108 due to its higher content of alloying elements that are responsible for the formation of hardening precipitates, as observed in Table 1.

The fatigue tests were started with the AA7046 samples in the machined-only or machined-and-polished conditions and later with the AA7108 only in the machined-and-polished condition. Fig. 14 contains the S–N curves for tests on machined-only or machined-and-polished samples to verify the effect of the surface finish on the fatigue behavior of the AA7046. The parameters that represent the fatigue curves correspond to 50% of the probability of failure. Fatigue tests were conducted up to fracture, except for points on the graph indicated by an arrow. Under these conditions, the test was interrupted with 10^7 cycles without having fractured. The black curve in Fig. 14 refers to the tests on the machined-only samples, and the red curve was obtained from fatigue tests on machined-and-polished samples. The roughness results for the aluminum alloy samples that had been machined-only or

Table 2 – Yield Strength (YS), Ultimate Tensile Strength (UTS), and elongation (E) values obtained in tensile and Brinell hardness (BH) tests of the AA7108 and AA7046 in the aged and solubilized condition.

	YS [MPa]	UTS [MPa]	E [%]	BH
AA 7108	292 ± 3	341 ± 2	12 ± 2	97 ± 4
AA 7046	416 ± 4	448 ± 4	14 ± 1	133 ± 3

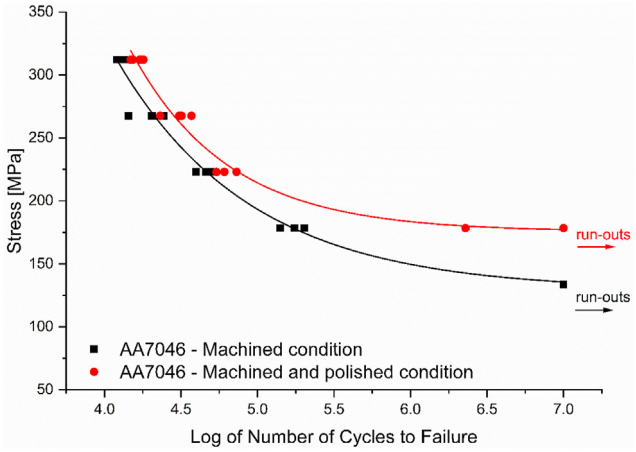

Fig. 14 – S–N curves obtained from fatigue tests of the AA7046 specimens under machined only and machined and polished conditions. Arrows indicate tests stopped after 10^7 cycles without fracturing.

Table 3 – Results of surface roughness measurement of the AA7046 specimens under machined only and machined and polished conditions.

Condition	R_a (μm)	R_q (μm)	R_z (μm)
Machined only	7.87	9.51	37.59
Machined and polished	0.25	0.32	1.86

machined-and-polished are provided in Table 3. The R_z scale (average value of the sum of the value from the largest peak to the largest valley) as a reference indicates that polishing promoted a significant decrease in the R_z roughness of the samples compared to the machined-only samples. The change in the mean value of R_z degreased from 37.59 μm in the machined-only condition to 1.86 μm in the machined-and-polished samples.

In general, the machined-and-polished samples presented a higher fatigue resistance than the machined-only samples. For high levels of maximum stress, the machined-only and machined-and-polished samples failed with 1.3×10^4 and 1.6×10^4 fatigue cycles, respectively. Note that the effect of surface finish was not as pronounced in fatigue tests with these applied stresses. The improvement in fatigue life became more evident as the maximum applied stress decreased. When the maximum stress was reduced to

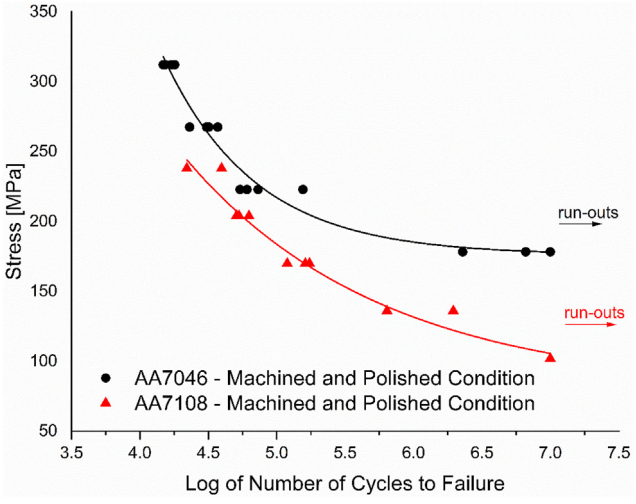

Fig. 15 – S–N curves from fatigue tests performed on specimens in the machined and polished condition for AA7046 and AA7108. The arrows indicate the tests interrupted after 10^7 cycles without fracturing.

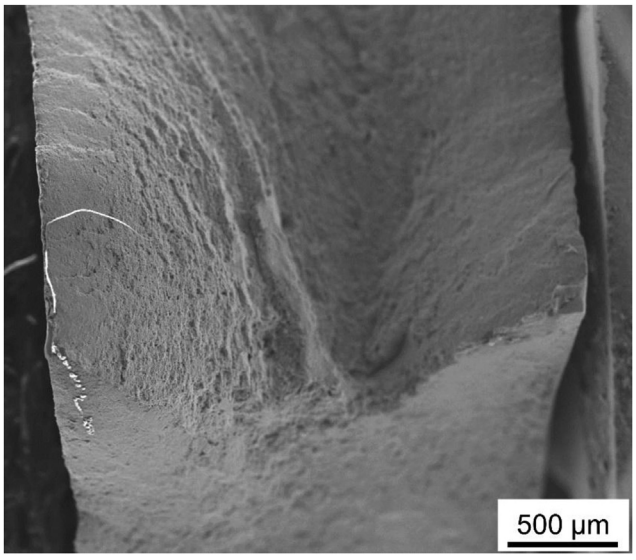

Fig. 16 – Fracture surface observed by SEM of a machined specimen of AA7046 fatigue tested with a maximum stress of 178.4 MPa and 202,729 cycles to failure.

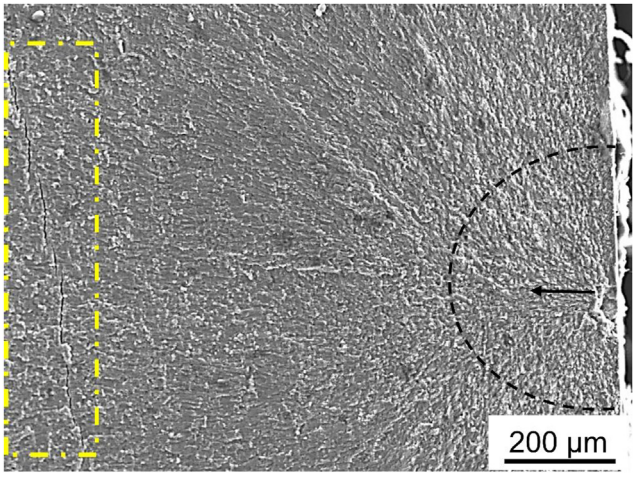

Fig. 17 – Fracture surface observed by SEM of a machined and polished AA7046 specimen fatigue tested with a maximum stress of 223 MPa and 155,354 cycles to failure, showing the region of crack initiation and propagation and the presence of secondary cracks.

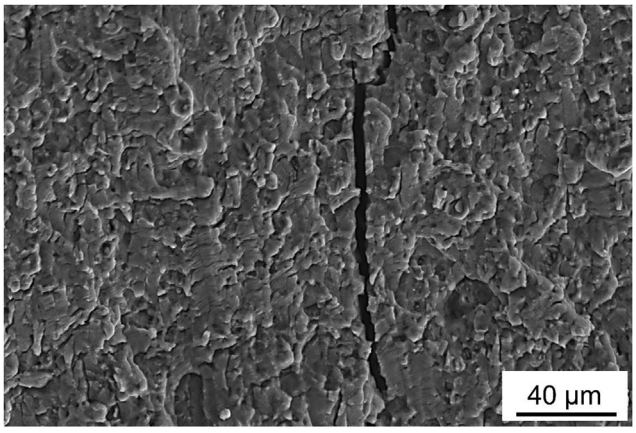

Fig. 18 – Fracture surface observed by SEM of a machined and polished AA7046 specimen fatigue tested with a maximum stress of 178.4 MPa and 2,287,754 cycles to failure, evidencing a deep secondary crack.

178 MPa, the fatigue life of the machined-and-polished sample withstood 10^7 cycles without fracturing, whereas the machined-only samples had 1.8×10^5 cycles. Surfaces with greater surface roughness had greater initiation and propagation of cracks during fatigue cycles. Several authors [18–22] have demonstrated the deleterious effect on fatigue resistance due to the increase in surface roughness. According to Curtis et al. [19], surface roughness accelerates nucleation and premature crack propagation. Jabur et al. [20] proposed empirical relationships to describe the reduction in fatigue life related to increased roughness. Li et al. [21] proposed an equation to obtain the stress concentration factor (K_t) from roughness measurements R_z (sum of the value of the largest peak to the largest valley) and the distances between adjacent peaks. Benedetti et al. [22] concluded surface roughness greatly impacts the mechanism of fatigue crack initiation and its early propagation. These authors also found that a surface

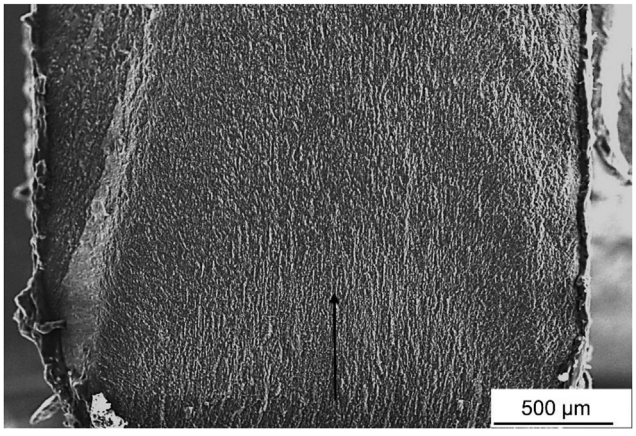

Fig. 19 – Fracture surface observed by SEM of a machined and polished AA7108 specimen fatigue tested with a maximum stress of 136 MPa and 1,953,600 cycles to failure, displaying the crack propagation direction.

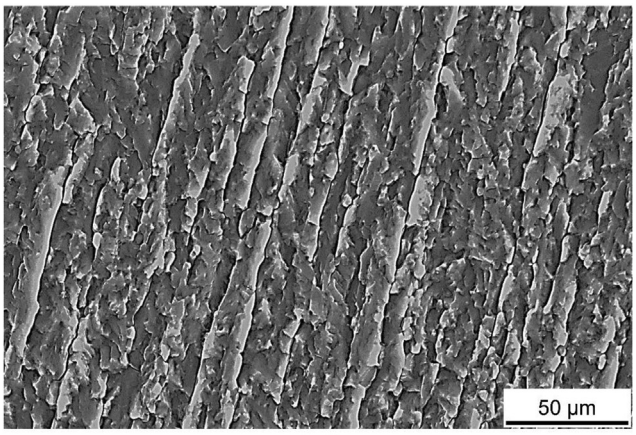

(A)

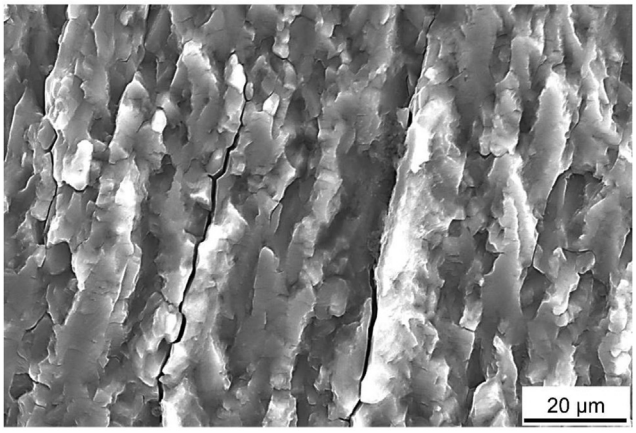

(B)

Fig. 20 – Details of the fracture surface observed by scanning electron microscopy in the crack propagation region of a machined and polished AA7108 specimen in fatigue tested with a maximum stress of 136 MPa and 1,953,600 cycles to failure, illustrating (A) the elongated grains in the crack propagation region and (B) secondary intergranular cracks.

finish by gentle grinding can minimize the effect of roughness. Borges et al. [18] showed that the surface roughness generated by shot peening affects the fatigue properties of the material.

Fig. 15 presents the S–N curves obtained from fatigue tests on machined-and-polished 7108 and AA7046 samples. The red curve was obtained from fatigue tests on AA7046 samples and the black curve on AA7108. As stated earlier, the dots on the graph accompanied by an arrow indicate test interruption with 10^7 cycles without fracturing. These curves evidence that the AA7046 has better fatigue properties than the AA7108. This is due to the greater amount of alloying elements responsible for precipitation hardening in the AA7046.

Figs. 16–23 illustrate the fracture surfaces observed by SEM of the fatigue tested samples. The characteristics of the fracture surface were similar for the two aluminum alloys (7046 and 7108) investigated under similar applied stress conditions and number of cycles to failure. Moreover, no significant

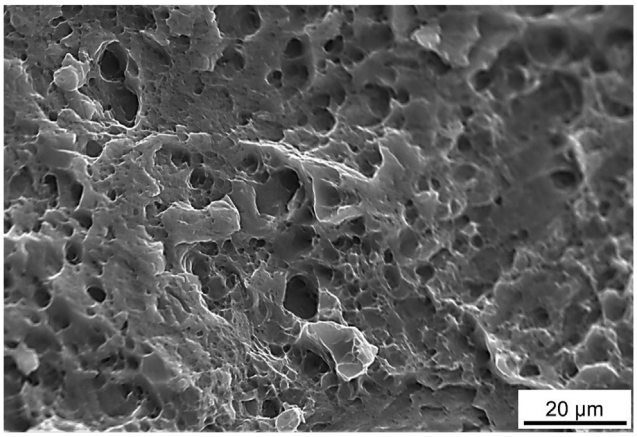

Fig. 21 – Final fracture surface rupture region observed by SEM of a machined and polished AA7108 specimen fatigue tested with a maximum stress of 136 MPa and 1,953,600 cycles to failure, showing a fracture mixed.

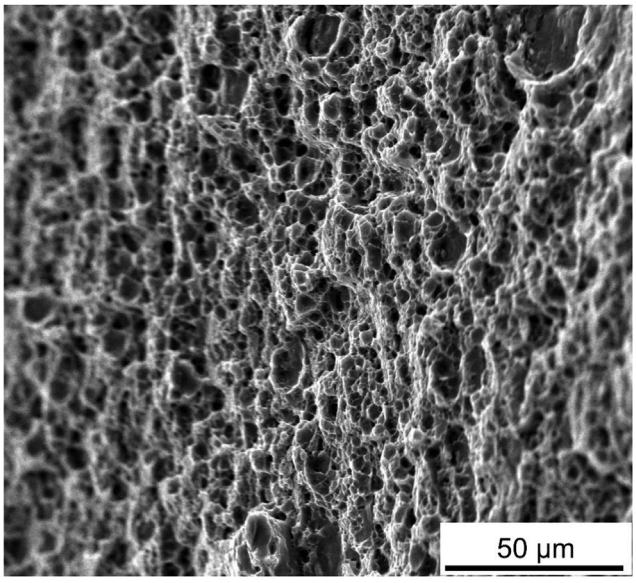

Fig. 23 – Fracture surface observed by SEM of a machined and polished AA7108 specimen fatigue tested with a maximum stress of 238 MPa and 39,571 cycles to failure, displaying a region with dimples.

differences in the aspects were observed in the fracture surfaces of machined-and-polished samples compared to the machined-only samples. In general, the fracture surfaces of the samples presented a typical characteristic of accentuated relief. After the initial growth of the crack in a plane almost perpendicular to the loading axis, a high slope of the fracture surface occurred. An example of this characteristic is visible in Fig. 16 and is in agreement with what Fintóv et al. [23] observed in fatigue studies of the 7075 aluminum alloy.

Fig. 17 shows the fracture surface region of the machined-and-polished AA7046 sample, fatigue tested with a maximum stress of 223 MPa and 155,354 cycles to failure. On this fracture surface, a region of crack initiation and propagation is indicated by the arrow. The crack advanced in a direction perpendicular to the elongated grains resulting from the extrusion process. The rectangular dashed region indicates a large and deep secondary crack, perpendicular to the direction of growth of the main crack. These secondary cracks were observed in the crack propagation region in all fatigue tested samples for both the AA7046 and AA7108. A detail of the crack propagation region of the machined-and-polished sample of 7046 fatigue tested with a maximum stress of 178.4 MPa and 2,287,754 cycles to failure is in Fig. 18. This figure details the presence of a flat surface with slight traces of plastic deformation, as observed in other works [1,24]. A deep secondary crack is also visible on this fracture surface.

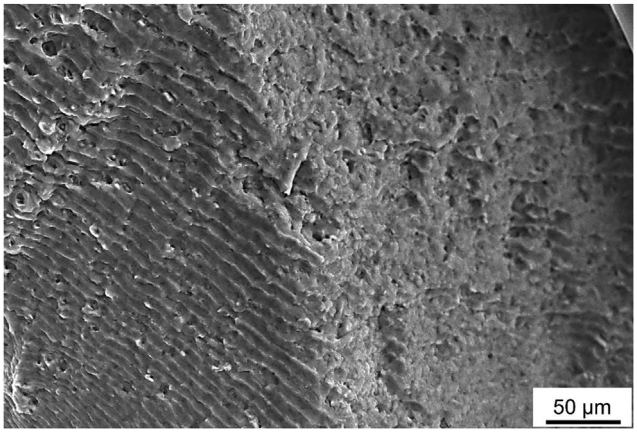

Fig. 22 – Fracture surface observed by SEM of a machined and polished AA7108 specimen fatigue tested with a maximum stress of 238 MPa and 39,571 cycles to failure, presenting a region with striations.

The rectangle in Fig. 17 indicates the beginning of the crack on the side of the sample, which is from the surface of the extruded profile. Fig. 19 exhibits the fracture initiation region from the thickness of the AA7108 sample fatigue tested with a maximum stress of 136 MPa and 1,953,600 cycles to failure. The arrow indicates in Fig. 19 the fractography in the direction of crack propagation from the surface to the interior of the sample. Amplification of the crack propagation region is presented in Fig. 20. In Fig. 20(A), the elongated grains resulting from the extrusion process can be clearly seen. Fig. 20(B) clearly illustrates the presence of a secondary crack along the contours of the extruded grains. The final region of rupture, shown in Fig. 21, contains a mixed fracture characterized by the presence of a transgranular fracture and dimples.

The fracture surfaces of the samples tested at higher stresses had a region with a smaller crack propagation area and a more extensive region of failure due to mechanical overload. The crack propagation region in the machined-and-polished AA7108 sample, fatigue tested with a maximum stress of 238 MPa and 39,571 cycles to failure, contains plastic deformation and the presence of striations perpendicular to the crack growth direction, as observed in Fig. 22. Chen et al. [25] also observed striations with these same characteristics in

the crack propagation region in fatigue tests of the series 7XXX alloys (Al–Zn–Mg–Cu–Zr). Fig. 23 exhibits the region of fracture due to mechanical overload of the same sample. This region presents dimples in a large extension of the fracture surface of this sample.

4. Conclusions

In this work, the microstructures of the AA7108 and AA7046 under casting, homogenized, extruded, solubilized, and aged conditions were analyzed. The performance in fatigue tests of samples extracted from the extruded profile was evaluated. In the cast AA7108, interdendritic microsegregation inside the grains was observed. Precipitated phases occurred almost completely at the grain boundaries. In the homogenization of the billets of this alloy, the precipitated phases dissolved. These precipitated phases were less and smaller than observed in the as-casted condition in all regions of the billet. The AA7046, in the as-casted condition, displayed shrinkage microvoids throughout the length of the billet and a microstructure of heterogeneous grains, with the presence of a remelted layer at a maximum depth of 10 mm. The effect of the surface finish of the sample on fatigue performance was more pronounced at low levels of maximum stress and a high number of cycles to failure. The AA7046 showed better tensile and fatigue properties than the AA7108. In medium and high cycle fatigue tests of the AA7108 and AA7046, the cracks advanced in a direction perpendicular to the elongated grains resulting from the extrusion process. On all fracture surfaces, deep secondary cracks were observed perpendicular to the growth direction of the main crack. In the propagation region, elongated grains resulting from the extrusion process were also present. Along the contours of the extruded grains, the presence of these secondary cracks was noted. The fracture surfaces of the samples tested with a high number of cycles displayed a region with a smaller crack propagation area and a more extensive region of rupture due to mechanical overload. The crack propagation region was characterized by plastic deformation and the presence of striations perpendicular to the growth direction.

Declaration of Competing Interest

The authors declare that they have no known competing financial interests or personal relationships that could have appeared to influence the work reported in this paper.

Acknowledgements

The authors are grateful for the research support from Comissão Nacional de Energia Nuclear and its scholarship given to G.F.C. Almeida [grant n°01342.003512/2019]. They also received the financial support from Institutional Internationalization Project UPM/CAPES PrInt, Research Productivity Scholarship, CNPq: 306956/2018-7 and DAI Program - CNPq notice 2018: 443828/2018-0. The authors also thank the Laboratório Metalográfico da Companhia Brasileira do Alumínio (CBA) for the sample preparation for optical microscopy.

REFERENCES

[1] Stanzl-Tschegg SE, Meischel M, Arcari A, Iyyer N, Apetre N, Phan N. Combined cycle fatigue of 7075 aluminum alloy – fracture surface characterization and short crack propagation. Int J Fatig 2016;91:352–62.
[2] Xue Y, McDowell DL, Horstemeyer MF, Dale MH, Jordon JB. Microstructure-based multistage fatigue modeling of aluminum alloy 7075-T651. Eng Fract Mech 2007;74:2810–23.
[3] Baragetti S, Borzini E, Božic Z, Arcieri EV. On the fatigue strength of uncoated and DLC coated 7075-T6 aluminum alloy. Eng Fail Anal 2019;102:219–25.
[4] Dixon B, Molent L, Barter S. A study of fatigue variability in aluminium alloy 7050-T7451. Int J Fatig 2016;92:130–46.
[5] Gupta RK, Anil Kumar V, Sarath Krishnan A, Niteshraj J. Hot deformation behavior of aluminum alloys AA7010 and AA7075. J Mater Eng Perform 2019;28:5021–36.
[6] Jin N, Zhang H, Han Y, Wu W, Chen J. Hot deformation behavior of 7150 aluminum alloy during compression at elevated temperature. Mater Char 2009;60:530–6.
[7] Mirzadeh H. Simple physically-based constitutive equations for hot deformation of 2024 and 7075 aluminum alloys. Trans Nonferrous Met Soc China 2015;25:1614–8.
[8] Mirzadeh H. Constitutive description of 7075 aluminum alloy during hot deformation by apparent and physically-based approaches. J Mater Eng Perform 2015;24:1095–9.
[9] Yang Y, Zhang Z, Li X, Wang Q, Zhang Y. The effects of grain size on the hot deformation and processing map for 7075 aluminum alloy. Mater Des 2013;51:592–7.
[10] Paulisch MC, Treff A, Driehorst I, Reimers W. The influence of natural aging and repeated solution annealing on microstructure and mechanical properties of hot extruded alloys Al 7020 and Al 7175. Mater Sci Eng A 2018;709:203–13.
[11] Zhang X, Huang Z, Chen B, Zhang Y, Tong J, Fang G, et al. Investigation on residual stress distribution in thin plate subjected to two sided laser shock processing. Opt Laser Technol 2019;111:146–55.
[12] Shin J, Kim T, Kim D, Kim D, Kim K. Castability and mechanical properties of new 7xxx aluminum alloys for automotive chassis/body applications. J Alloys Compd 2017;698:577–90.
[13] Paulisch MC, Lentz M, Wemme H, Andrich A, Driehorst I, Reimers W. The different dependencies of the mechanical properties and microstructures on hot extrusion and artificial aging processing in case of the alloys Al 7108 and Al 7175. J Mater Process Technol 2016;233:68–78.
[14] Xu DK, Birbilis N, Lashansky D, Rometsch PA, Muddle BC. Effect of solution treatment on the corrosion behaviour of aluminium alloy AA7150: optimisation for corrosion resistance. Corros Sci 2011;53:217–25.
[15] Rometsch Pa, Zhang Y, Knight S. Heat treatment of 7xxx series aluminium alloys—some recent developments. Trans Nonferrous Met Soc China 2014;24:2003–17.
[16] Xu DK, Rometsch PA, Birbilis N. Improved solution treatment for an as-rolled Al–Zn–Mg–Cu alloy. Part II. Microstructure and mechanical properties. Mater Sci Eng A 2012;534:244–52.
[17] Xu DK, Birbilis N, Rometsch PA. Effect of S-phase dissolution on the corrosion and stress corrosion cracking of an as-rolled Al-Zn-Mg-Cu alloy. Corros J Sci Eng 2012;68. 035001-1-035001–10.

[18] Borges AAC, de Araújo MC, Couto AA, de Lima NB, Contatori C. Evaluation of the residual stress and microstructure of extruded and shot peened aluminum alloy 6082. Mater Sci Forum 2018;930:507–12.
[19] Curtis S, De Los Rios ER, Rodopoulos CA, Levers A. Analysis of the effects of controlled shot peening on fatigue damage of high strength aluminium alloys. Int J Fatig 2002;25:59–66.
[20] Jabur KS. Analysis of the effects of aggressive shot peening on fatigue life of 7075 – T6 aluminum alloy. Al-Khwarizmi Eng J 2012;8:90–5.
[21] Li JK, Mei Y, Duo W, Renzhi W. An analysis of stress concentrations caused by shot peening and its application in predicting fatigue strength. Fatig Fract Eng Mater Struct 1992;15:1271–9.
[22] Benedetti M, Fontanari V, Bandini M, Savio E. High- and very high-cycle plain fatigue resistance of shot peened high-strength aluminum alloys: the role of surface morphology. Int J Fatig 2015;70:451–62.
[23] Fintová S, Kuběna I, Trško L, Horník V, Kunz L. Fatigue behavior of AW7075 aluminum alloy in ultra-high cycle fatigue region. Mater Sci Eng A 2020:774.
[24] Kowalski A, Ozgowicz W, Grajcar A, Lech-Grega M, Kurek A. Microstructure and fatigue properties of AlZn6Mg0.8Zr alloy subjected to low-temperature thermomechanical processing. Metals (Basel) 2017;7:448.
[25] Chen L, Yan A, Liu Hs, Li Xq. Strength and fatigue fracture behavior of Al–Zn–Mg–Cu–Zr(–Sn) alloys. Trans Nonferrous Met Soc China 2013;23:2817–25.